

Article

Negatively charged organic–inorganic hybrid silica nanofiltration membranes for lithium extraction

Xiaoxian Wu, Haoyue Liu, Yibin Wei, Ying Fei, Hong Qi*

State Key Laboratory of Material-Oriented Chemical Engineering, Membrane Science and Technology Research Center, Nanjing Tech University, Nanjing 210009, China

ARTICLE INFO

Article history:

Received 2 August 2019

Received in revised form 11 October 2019

Accepted 1 November 2019

Available online 9 November 2019

Keywords:

Nanofiltration

Membrane

BTESE

Water lithium resource

Lithium recovery

ABSTRACT

Effective extraction of lithium from high Mg^{2+}/Li^+ ratio brine lakes is of great challenge. In this work, organic–inorganic hybrid silica nanofiltration (NF) membranes were prepared by dip-coating a 1,2-bis(triethoxysilyl)ethane (BTESE)-derived separation layer on tubular TiO_2 support, for efficient separation of $LiCl$ and $MgCl_2$ salt solutions. We found that the membrane calcinated at $400\text{ }^\circ\text{C}$ (M1–400) could exhibit a narrow pore size distribution (0.63–1.66 nm) owing to the dehydroxylation and the thermal degradation of the organic bridge groups. All as-prepared membranes exhibited higher rejections to $LiCl$ than to $MgCl_2$, which was attributed to the negative charge of the membrane surfaces. The rejection for $LiCl$ and $MgCl_2$ followed the order: $LiCl > MgCl_2$, revealing that Donnan exclusion effect dominated the salt rejection mechanism. In addition, the triple-coated membrane calcinated at $400\text{ }^\circ\text{C}$ (M3–400) exhibited a permeability of about $9.5\text{ L}\cdot\text{m}^{-2}\cdot\text{h}^{-1}\cdot\text{bar}^{-1}$ for $LiCl$ or $MgCl_2$ solutions, with rejections of 74.7% and 20.3% to $LiCl$ and $MgCl_2$, respectively, under the transmembrane pressure at 6 bar. Compared with the previously reported performance of NF membranes for Mg^{2+}/Li^+ separation, the overall performance of M3–400 is highly competitive. Therefore, this work may provide new insight into designing robust silica-based ceramic NF membranes with negative charge for efficient lithium extraction from salt lakes.

© 2019 The Chemical Industry and Engineering Society of China, and Chemical Industry Press Co., Ltd.
All rights reserved.

1. Introduction

As the lightest element in nature, lithium is widely utilized in various fields such as ceramics [1,2], pharmaceuticals, and rechargeable batteries. [3,4] In addition to Li-containing ores, lithium resources mainly exist as the ionic form (*i.e.* Li^+) in salt lakes [5]. It is estimated that lithium reserves are 0.54 million tons in China, but about 85% of them are stored as brine lithium in salt lakes [6]. Therefore, extraction of Li^+ from salt lakes has attracted much interest to meet the growing demand for lithium usage. However, due to the high Mg^{2+}/Li^+ ratio (*i.e.* the concentration of Li^+ is $\sim 0.3\text{ g}\cdot\text{L}^{-1}$ and the ratio of Mg^{2+}/Li^+ is ~ 48.5) and the existence of other salt ions (*e.g.* Na^+) in salt lakes [7], development of efficient strategies for selective extraction of Li^+ remains challenging.

Recently, approaches such as chemical precipitation, lithium ion-sieve (LIS) adsorption and solvent extraction have been explored [8,9]. Among them, chemical precipitation is only applicable for the cases with a low ratio of Mg^{2+}/Li^+ of brine or high capacity of Li^+ [10]. Despite owing good adsorption capacity for Li^+ , LISs generally suffer from poor structural stability caused by dissolution loss [11]. In contrast, membrane-based technologies have demonstrated their technical

merits including high efficiency and low energy consumption in water treatment including desalination [12] and drinking water purification [13]. Nanofiltration (NF), a pressure-driven separation process with tunable ionic sieving performance, has been considered as a promising alternative to conventional lithium extraction approaches [14].

Yang *et al.* [15] investigated the feasibility of Mg^{2+}/Li^+ separation by using commercial Desal DK NF membranes (GE Osmonics). The Mg^{2+}/Li^+ separation factor (*i.e.* $(C[Mg^{2+}]/C[Li^+])_{\text{permeation}}/(C[Mg^{2+}]/C[Li^+])_{\text{retention}}$) in their study was 0.31, and they believed that intrapore charge density of the membranes play a dominant role in selective Mg^{2+}/Li^+ separation. Subsequently, Bi *et al.* [16] further investigated a series of effects (*e.g.* salt concentration, transmembrane pressure, introduction of K^+ or Na^+) on Mg^{2+}/Li^+ separation performance using spiral-wound DK NF membranes and their results revealed that the Mg^{2+}/Li^+ selectivity was dominated by Donnan exclusion effect. Wu *et al.* [17] found that their negatively charged polyamide/poly(phthalazinone ether sulfone ketone) (PA/PPEsk) NF membrane could show much higher rejection to Li^+ than to Mg^{2+} , confirming that negatively charged NF membranes might be used for efficiently separation of Li^+/Mg^{2+} mixture.

However, these polymeric NF membranes usually suffer from poor chlorine resistance and severe fouling [18], which limits their practical applications in brine lakes for Li^+ extraction. Owing to excellent chemical stability and regeneration property, robust ceramic NF membranes

* Corresponding author.
E-mail address: hqi@njtech.edu.cn (H. Qi).

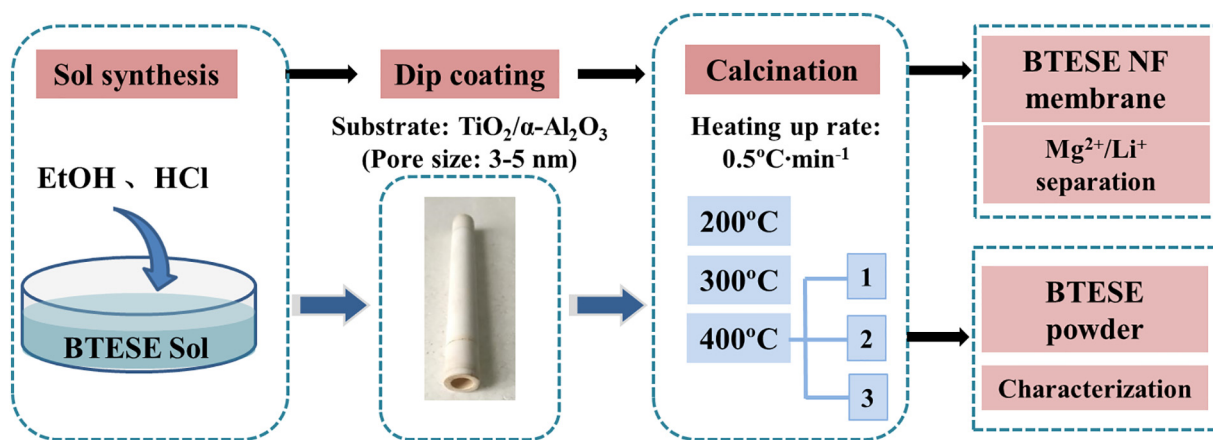


Fig. 1. Schematic illustration of (a) the coating setup and (b) sol-gel based membrane preparation process.

have gained much popularity for producing high value-added products [19]. In ceramic membrane family, organic-inorganic hybrid silica membranes consisting of organic Si-C_n-Si bridges and inorganic Si-O-Si bonds have attracted considerable attention for their excellent performance in the applications of gas separation, pervaporation, reverse osmosis (RO), and membrane reactors [20–22]. In the past decade, 1,2-bis(triethoxysilyl)ethane (BTESE)-derived organic-inorganic hybrid silica membranes with controllable microporous structures have been proved with good hydrothermal stability and excellent chemical resistance over pure silica membranes. Despite these technical merits, to our best knowledge, BTESE-derived NF membranes for selective separation of monovalent/divalent salt solutions lack investigation.

As the pore structures of BTESE-derived hybrid silica membranes can be effectively tailored for salt rejection and the membranes are easy for industrial large-scale production via sol-gel method, BTESE-derived organic-inorganic hybrid networks are attractive to be constructed as NF membranes for Li⁺ extraction from brine lake with high Li⁺/Mg²⁺ ratio. Here, we aim to prepare BTESE-derived organic-inorganic hybrid NF membrane with favorable surface charge by sol-gel method for effective lithium extraction through selectively separating LiCl and MgCl₂ salt solutions. To obtain appropriate microporous structure, sol-gel chemistry and calcination process were carefully controlled to prepare the BTESE-derived NF membranes. The effects of calcination temperature and coating time on the structural changes and salt rejection performance of the as-prepared membranes were

investigated by various characterization techniques and salt rejection experiments.

2. Experimental

2.1. Preparation of sols and gel powders

1,2-Bis(triethoxysilyl)ethane (BTESE) from ABCR was used as the precursor. Ethanol (anhydrous) was purchased from Merck. Nitric acid (HNO₃, 65 wt%) was purchased from Lingfeng in Shanghai. Prior to further use, the concentrated nitric acid was diluted to 0.1 M using deionized (DI) water.

Organic-inorganic hybrid silica sols were prepared by the following procedure. First, 5 ml BTESE and 13 ml ethanol were well mixed under nitrogen atmosphere within a glovebox. Meanwhile, 0.67 ml diluted nitric acid solution was mixed with 2.7 ml DI water in a 50 ml beaker, and then, the mixture was drop-wise added into the as-prepared BTESE-ethanol mixture under vigorous stirring (120 r·min⁻¹) in an ice bath. Along with continuous stirring, the final mixture was refluxed in a water bath at 60 °C for 90 min.

Dried flake gels were obtained by drying the corresponding sols for 8 h at room temperature. The obtained gels were then ground into fine powders followed by a thermal treatment under N₂ atmosphere. The calcination procedure includes a heating up and cooling down process at a rate of 0.5 °C·min⁻¹, with dwelling time of 3 h at 200, 300 and

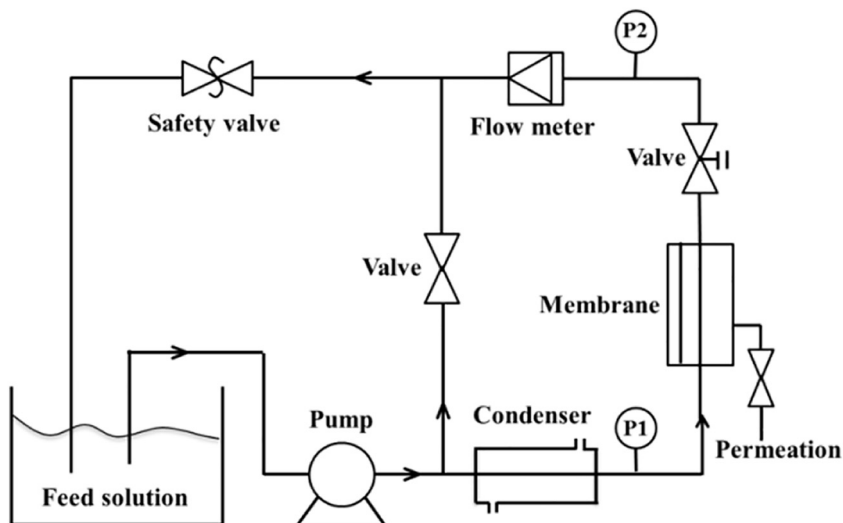


Fig. 2. Schematic diagram of the experimental apparatus for the measurement of NF performance.

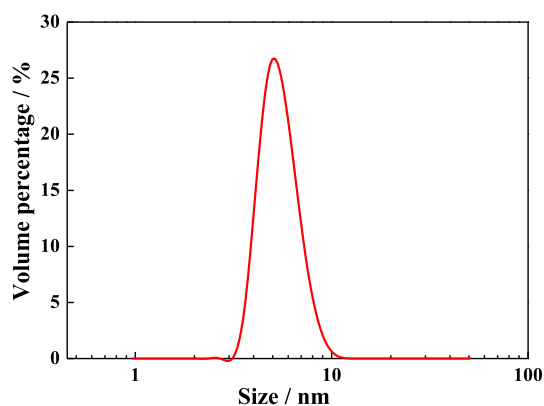


Fig. 3. Particle size distribution of the as-prepared BTESE-derived sol.

Table 1
Pore structure data of P-200, P-300 and P-400

Powders	$S_{\text{BET}}/\text{m}^2\cdot\text{g}^{-1}$	Pore volume/ $\text{cm}^3\cdot\text{g}^{-1}$
P-200	302.6	0.160
P-300	221.4	0.116
P-400	166.7	0.087

400 °C, respectively. The powder samples were marked as P-200, P-300 and P-400, accordingly, where the specific numbers refer to the calcination temperature.

2.2. Fabrication of membranes

To prepare BTESE-derived organic–inorganic hybrid silica membranes, the as-prepared BTESE sols were diluted to a solution of 0.17 M Si in concentration. Then, the diluted sols were coated on tubular TiO_2 membranes (pore size: 5 nm, outer diameter: 10 mm; inner diameter: 8 mm, length: 105 mm, Nanjing Hongyi Ceramic Membranes Co. Ltd., China) by dip-coating method. Fig. 1 shows the schematic diagram of the coating setup and sol–gel based membrane preparation process. In this process, the pulling speed and dwelling time were kept at $0.5\text{ cm}\cdot\text{s}^{-1}$ and 60 s, respectively. Then the coated membranes were dried in an oven at a temperature of 60 °C for 3 h. Subsequently, the membranes were calcined under N_2 atmosphere in a tube furnace. It should be noted that the calcination process is the same as the calcination process for gel powders. The integrated coating–calcination process could be repeated for various times in this study. According to coating time and calcination temperature, the as-prepared membranes were named M1–200, M1–300, M1–400, M2–400 and M3–400, respectively.

M refers to membrane and the number followed by M (i.e. 1, 2 and 3) represents coating time. 200, 300 and 400 represent the calcination temperature.

2.3. Characterization

The microporous structure of powders was analyzed by N_2 adsorption–desorption isotherms with a physical gas sorption instrument (ASAP 2460, Micromeritics) at 77 K. Prior to measurements, the samples were degassed under vacuum at 473 K for 12 h. The pore size distribution was calculated based on non-local density functional theory (NLDFT). X-ray photoelectron spectroscopy (XPS) and Fourier transform infrared (FTIR) spectroscopy were used to study the chemical states of the as-prepared membranes. Zeta potential of the powders in LiCl and MgCl_2 solutions with different pH values were measured with a zeta potential analyzer (Zetasizer Nano ZS90, Malvern). For zeta potential measurement, 0.03 g P-400 samples were dispersed into 50 ml salt solution ($2\text{ mmol}\cdot\text{L}^{-1}$) and $0.1\text{ mol}\cdot\text{L}^{-1}$ HCl or $\text{NH}_3\cdot\text{H}_2\text{O}$ solution was used to adjust pH of the solution. Surface wettabilities of the as-prepared membranes were studied through a contact angle analyzer (A-100P, MAIST, China). The surface and cross-sectional morphology of the as-prepared membranes were observed by scanning electron microscopy (SEM, S4800, Hitach, Japan). The elemental analysis of the membrane separation layer was performed by X-ray energy-dispersive spectrometry (EDS).

2.4. Evaluation of membrane performance

The NF performance of the as-prepared membranes was evaluated by a home-made cross-flow filtration system (Fig. 2). The crossflow velocity was remained up to $2\text{ m}\cdot\text{s}^{-1}$ at 18 °C to minimize the effect of concentration polarization on the feed side. The permeation flux (J_v) was calculated according to the following equation:

$$J_v = \frac{V}{A \times t} \quad (1)$$

where V is the total volume of the permeate through the membrane, A is the membrane area (21.35 cm^2), and t denotes the operation time.

The permeability was obtained by linear fitting to the value of flux over transmembrane pressure.

The concentration of permeate and feed solutions was analyzed by conductivity meter (DDS-307, Shanghai Leici Instrument Factory). The rejection (R) of salt was calculated as follows:

$$R = \left(1 - \frac{C_p}{C_f}\right) \times 100\% \quad (2)$$

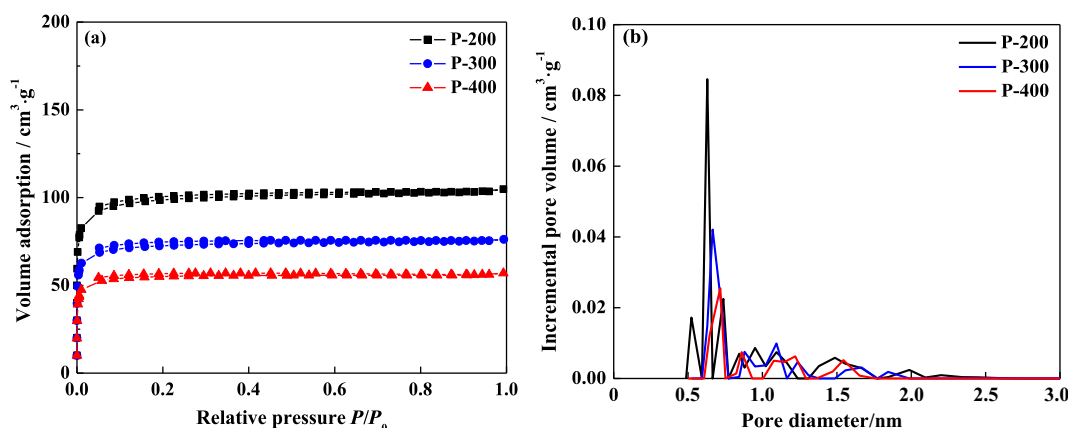


Fig. 4. (a) N_2 adsorption–desorption isotherms and (b) pore size distributions of P-200, P-300 and P-400.

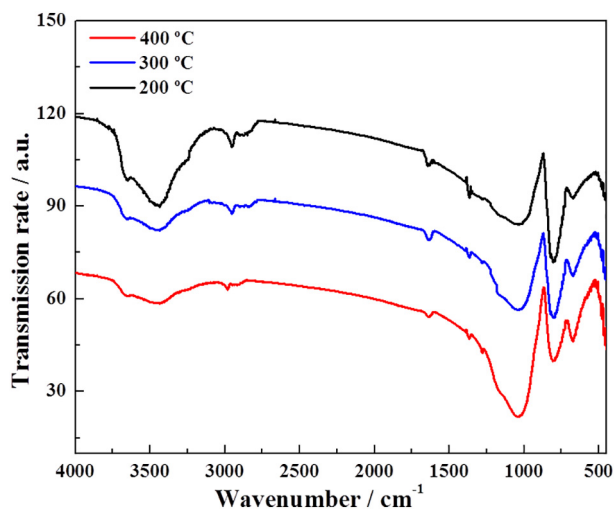


Fig. 5. FTIR spectra of P-200, P-300, and P-400.

where C_p and C_f are the concentration of permeate and feed solutions, respectively. $2 \text{ mmol}\cdot\text{L}^{-1}$ LiCl or $2 \text{ mmol}\cdot\text{L}^{-1}$ MgCl₂ solutions were prepared as the feed solutions.

3. Results and Discussion

3.1. Characterization of sols and gel powders

The sol–gel chemistry plays a crucial role in the ultimate membrane structure and properties [23]. The sol needs to be carefully tuned prior to coating for avoiding sol permeation into the TiO₂ support beneath. Fig. 3 shows the particle size distribution of the BTESE-derived sol prepared in this study. It can be seen that the sol exhibits a narrow unimodal distribution with a mean particle size about *ca.* 5 nm. Because the mean pore size of TiO₂ support is 5 nm, the as-prepared sol can be used for further membrane preparation.

To study the pore structure of the as-prepared BTESE-derived membranes, N₂ adsorption–desorption experiments for the gel powders calcined at 200, 300 and 400 °C were conducted. The pore structure data derived from the N₂ adsorption–desorption experiments are presented in Table 1. Fig. 4 shows the N₂ adsorption–desorption isotherms and pore size distributions of the obtained gel powders. All three samples exhibit the type I adsorption isotherm, indicating that the BTESE-derived networks have typical microporous structure (Fig. 4a). In Table 1, P-200 has a Brunauer–Emmett–Teller (BET) surface area of $302.6 \text{ m}^2\cdot\text{g}^{-1}$ and a pore volume of $0.160 \text{ cm}^3\cdot\text{g}^{-1}$, while the BET surface area and the pore volume of P-400 dramatically decrease to $166.7 \text{ m}^2\cdot\text{g}^{-1}$ and $0.087 \text{ cm}^3\cdot\text{g}^{-1}$, respectively. These results suggest that a higher calcination temperature leads to a denser structure of BTESE-derived hybrid silica network, which agrees with our previous work [24]. According to the hysteresis loops found in N₂ adsorption–

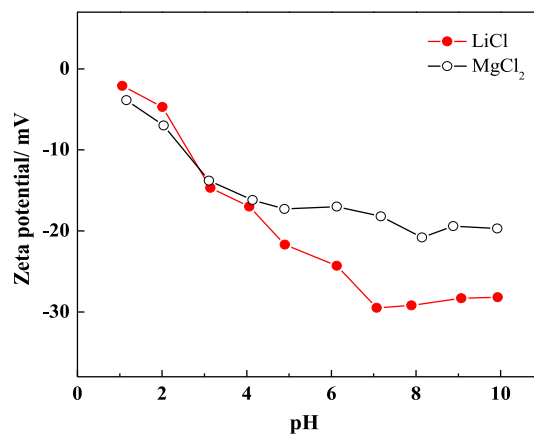


Fig. 7. Zeta potential of BTESE-derived membranes in LiCl and MgCl₂ solutions under various pH values.

desorption isotherm of the three samples, a small number of mesopores existed in these BTESE-derived microporous membranes [25].

To further explore the pore structure of the as-prepared membranes, the pore size distributions of the P-200, P-300 and P-400 were analyzed using the NLDFT model. As shown in Fig. 4b, the pore size of the three samples mainly distributed within the range of 0.5–2 nm. This result confirms that the as-prepared membranes have microporous structures, which matches with the pore size characteristics of typical NF membrane. In addition, the P-400 powders have a narrower pore size distribution than that of the P-300 and P-200 powders. The pore size distribution of the P-200 is between 0.5 and 2.6 nm while that of P-400 is narrower (0.63–1.66 nm). This indicates that higher calcination temperature leads to a higher cross-linking degree for a BTESE-derived network, resulting in more concentrated pore size distribution and smaller pore size of the BTESE-derived networks.

Fig. 5 shows the FTIR spectra of P-200, P-300 and P-400, which indirectly reflects the chemical structures of the hybrid silica networks in the M1-200, M1-300 and M1-400 membranes. A clear absorption band appears at 1040 cm^{-1} which is assigned to the asymmetric stretching vibration of the Si–O–Si groups [26]. It is well-known that silanol groups would condense to form a Si–O–Si network (*i.e.* dehydroxylation process) during the calcination process. The broad absorption band at 3450 cm^{-1} can be ascribed to the stretching vibrations of hydroxyl groups in the silanol groups (Si–OH). The characteristic peak for Si–OH was the strongest when the calcination temperature is 200 °C (P200), but the relative intensities of Si–OH characteristic peak decreased with the increase of calcination temperature. This suggests that a higher calcination temperature could lead to an enhanced dehydroxylation process (namely, a relatively higher cross-linking degree of the silica network). The characteristic peaks at around 700 cm^{-1} and 1410 cm^{-1} can be ascribed to Si–C stretching vibrations and CH₂ (in Si–CH₂–CH₂–Si) asymmetric bending vibrations,

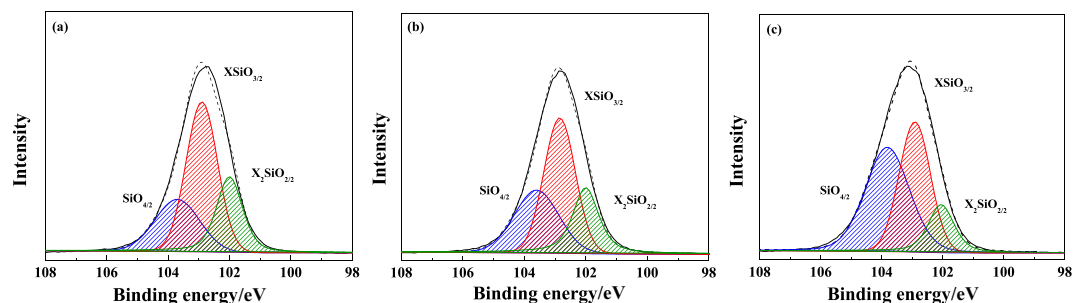


Fig. 6. Deconvolutions of the XPS Si 2p peaks of (a) P-200, (b) P-300 and (c) P-400 powders.

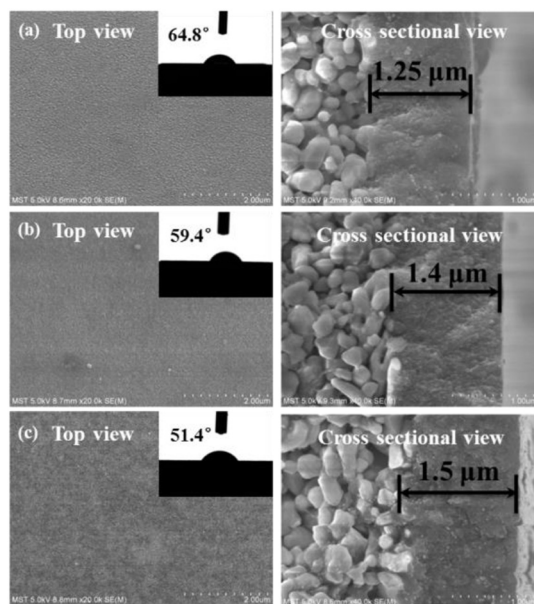


Fig. 8. Surface and cross-sectional SEM images of (a) M1–400, (b) M2–400 and (c) M3–400. The insets of surface SEM images of M1–400, M2–400 and M3–400 are water contact angles of the corresponding membrane surfaces.

respectively [27]. The relative intensities of the characteristic peak for Si–C and CH₂ decreased with the increase of the calcination temperature. This suggests that the thermal degradation of the organic bridged groups in the silica powders occurs at higher calcination temperatures.

Fig. 6 shows the Si 2p core-level spectra of P-200, P-300 and P-400 powders analyzed by XPS. The Si 2p peaks can be decoupled into three peaks corresponding to X₂SiO_{2/2} (102 eV), XSiO_{3/2} (102.8 eV) and SiO_{4/2} (103.7 eV), where X represents organic groups in organosilica [28]. The presence of the pure inorganic moiety (SiO_{4/2}) was caused by the decomposition of organic chains. The contents of SiO_{4/2} moiety in P-200, P-300 and P-400 are 24.5%, 30.3% to 46.8%,

respectively, which confirms that a higher calcination temperature results in much more SiO_{4/2} moiety formed in the networks.

As NF membrane surfaces are usually negatively or positively charged, different surface charges lead to different salt rejection performances. According to Donnan effect that salt rejection performance strongly depends on the surface charge of a NF membrane [29], thus the zeta potential measurements were carried out to investigate the surface charge property of the as-prepared BTESE-derived NF membranes in LiCl and MgCl₂ solutions with different pH values. Fig. 7 illustrates the zeta potential evolutions with pH of P-400 in 2 mmol·L⁻¹ LiCl and MgCl₂ solutions. P-400 exhibited negative zeta potential in either LiCl or MgCl₂ solution under the whole pH range. In the LiCl solution, the zeta potential values of P-400 decreased dramatically with the increase of pH. The zeta potentials of P-400 in MgCl₂ solution varying with pH showed a similar downwards tendency as that in LiCl solution, but the decrease was more moderate. It could be explained by the increasing degree of dissociating of hydrogen bond at high value of pH that more negative charge could be accumulated in the membrane surface [30]. Therefore, the charge repulsion between the as-prepared membrane and solution increases, which promotes the Donnan effect of membranes. It is worth noting that the zeta potential values of P-400 in LiCl solution was much lower than those in MgCl₂ solution when the pH value was above 7, indicating that the as-prepared BTESE-derived hybrid silica membrane surface could ionize more —OH in the LiCl solution. The as-prepared membrane exhibits stronger electronegativity in LiCl solution than that of MgCl₂ solution when pH is above 7, and this difference might be beneficial for separating LiCl and MgCl₂ in brine.

3.2. BTESE-derived hybrid silica NF membranes

The surface and cross-sectional morphologies of the as-prepared BTESE-derived NF membranes were imaged by SEM (Fig. 8). From the top view of the SEM images, M1–400, M2–400 and M3–400 show similar surface morphologies with no visible cracks or defects. Surface wettability is an important property for a membrane [31–33]. The insets in surface SEM images show the water contact angles of M1–400, M2–400

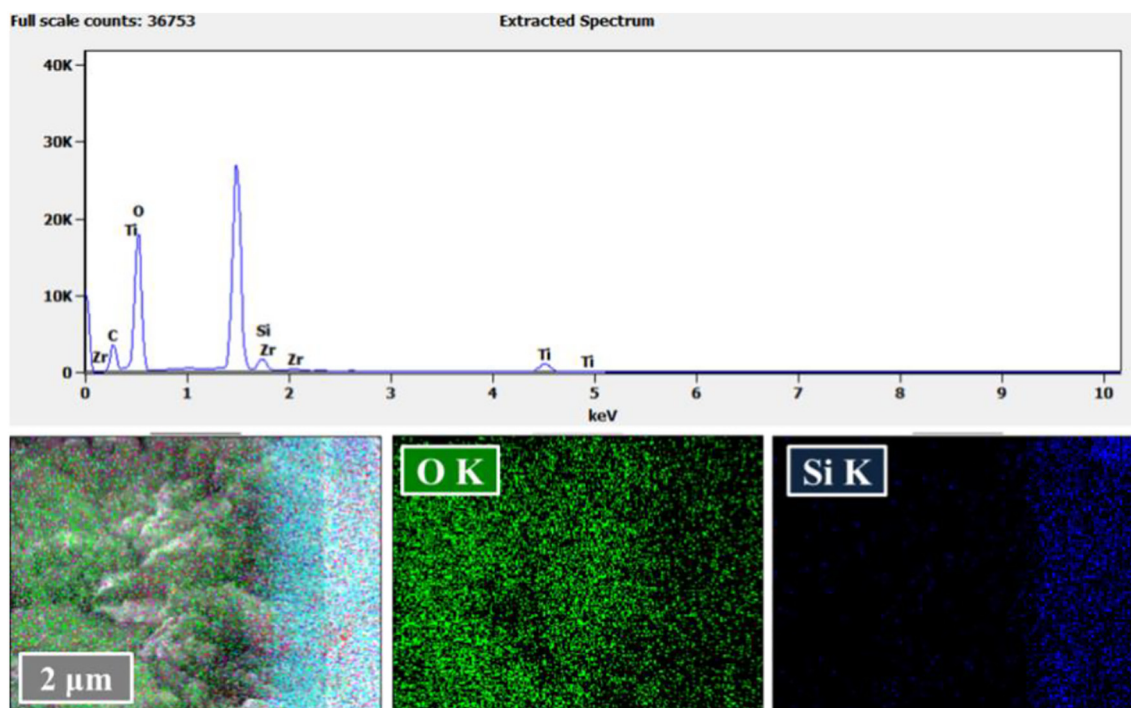


Fig. 9. EDS spectra analysis of M3–400.

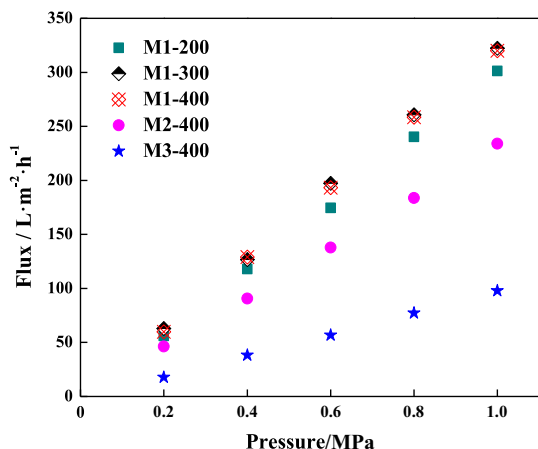


Fig. 10. The pure water flux of the as-prepared membranes as a function of transmembrane pressures.

and M3-400 membrane surfaces, respectively. M1-400 membrane had the highest water contact angle value, while M3-400 membrane showed the highest hydrophilicity. In the cross-sectional view, the thickness of top layers for M1-400, M2-400 and M3-400 membranes are 1.25, 1.4 and 1.5 μm , respectively. This indicates the thickness of BTESE-derived layer can slightly increase along with the increase of coating time.

To study the uniformity of the as-prepared membranes, the EDS-mapping analysis was conducted for the separation layer of M3-400 membrane (Fig. 9). According to the elemental analysis, we observed that O element could be found in both supporting layer and separation layer and Si element is uniformly dispersed in separation layer, confirming that the separation layer consists of Si and O. In addition, very rare Si dots could be found in the supporting layer, which suggests that very small amount of BTESE-derived sol may penetrate into the supporting layer in the coating process.

Fig. 10 shows pure water flux (J_v) of the as-prepared membranes as a function of transmembrane pressure. The permeate flux of the five membranes increases linearly to the applied pressure. The pure water permeabilities of M1-200, M1-300 and M1-400 were similar (293, 322 and 317 $\text{L}\cdot\text{m}^{-2}\cdot\text{h}^{-1}\cdot\text{MPa}^{-1}$, respectively). The pure water permeabilities of M2-400 and M3-400 membranes were 230 and 95 $\text{L}\cdot\text{m}^{-2}\cdot\text{h}^{-1}\cdot\text{MPa}^{-1}$, respectively. It was found that calcination temperature had nearly no effect on the pure water permeabilities of the corresponding membranes, while coating time significantly influenced the pure water permeability that more coating times resulted in lower pure water permeability. As evidenced by SEM images, the thickness of BTESE-derived separation layer increased with increasing the coating time, resulting in the rise of resistance.

Table 2 lists the pure water and 2 $\text{mmol}\cdot\text{L}^{-1}$ LiCl or MgCl_2 aqueous solution permeabilities of the five BTESE-derived hybrid silica NF membranes prepared by different calcination temperatures and coating times. The five membranes exhibited similar permeabilities when treating LiCl or MgCl_2 solutions compared with those for pure water. This result indicates that osmotic pressure effects caused by the salt solutes are negligible when the concentration of LiCl or MgCl_2 solutions is 2 $\text{mmol}\cdot\text{L}^{-1}$.

Fig. 11 shows the rejection performance of M1-200, M1-300 and M1-400 to LiCl and MgCl_2 under different transmembrane pressure. Under the applied transmembrane pressures of 0.2–1.0 MPa, the rejections of the three membranes to MgCl_2 were below 10%, while those to LiCl were around 20% with some fluctuations. These results suggest that calcination temperature for BTESE-derived hybrid silica membrane preparation has no obvious influence on rejections to LiCl and MgCl_2 salt solutions or there are some defects existed in the three membranes. In addition, the order of rejections to LiCl and MgCl_2 solutions did not follow the size order of the hydrated ions (Table 3) [34], but it agreed well with previous reports for Donnan exclusion theory of negatively charged NF membranes [35,36].

To investigate the effect of coating time on rejection performance of the prepared membranes to LiCl and MgCl_2 salt solutions, the rejection performance of M1-400, M2-400 and M3-400 to LiCl and MgCl_2 as a

Table 2
Pure water and 2 $\text{mmol}\cdot\text{L}^{-1}$ LiCl or MgCl_2 aqueous solution permeabilities of the as-prepared membranes

Membranes	Pure water permeability/ $\text{L}\cdot\text{m}^{-2}\cdot\text{h}^{-1}\cdot\text{MPa}^{-1}$	LiCl solution permeability/ $\text{L}\cdot\text{m}^{-2}\cdot\text{h}^{-1}\cdot\text{MPa}^{-1}$	MgCl_2 solution permeability/ $\text{L}\cdot\text{m}^{-2}\cdot\text{h}^{-1}\cdot\text{MPa}^{-1}$
M1-200	293	292	289
M1-300	322	295	315
M1-400	317	322	335
M2-400	230	218	234
M3-400	95	91	95

Note: the permeabilities were given based on the average of five experiments under pressure = 0.2, 0.4, 0.6, 0.8 and 1.0 MPa.

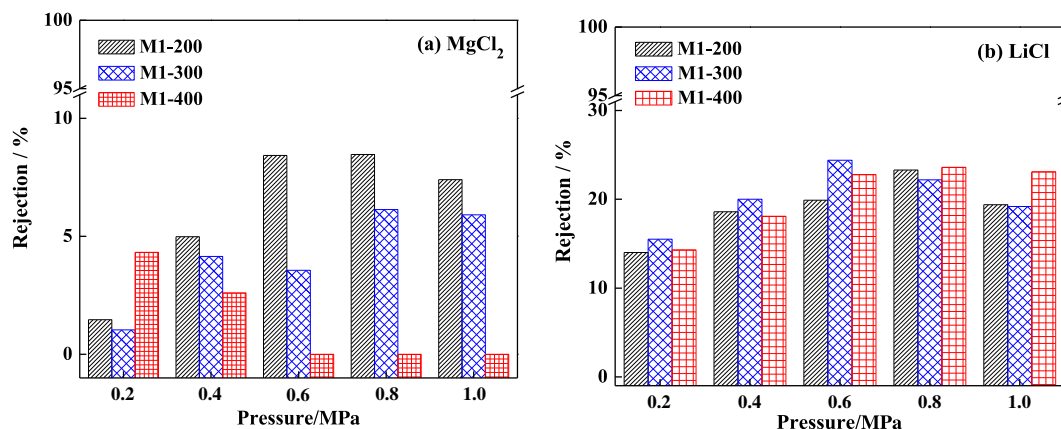


Fig. 11. Rejections of the M1-200, M1-300 and M1-400 membranes to (a) MgCl_2 and (b) LiCl as a function of the transmembrane pressure.

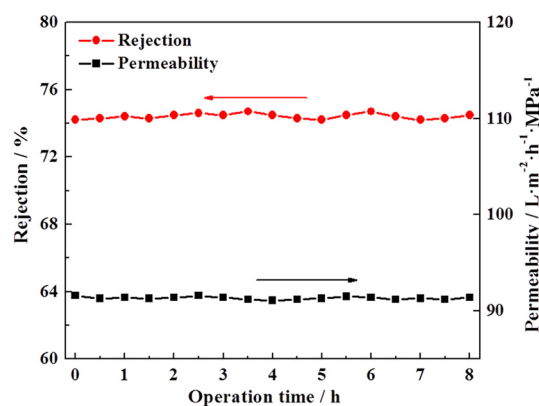
Table 3
Radii of hydrated ions [34]

Ions	Li ⁺	Mg ²⁺	Cl ⁻
Ion radius/nm	0.094	0.072	0.164
Hydrated radius/nm	0.382	0.428	0.332

function of the applied transmembrane pressure are given in Fig. 12. It was obvious that the rejections of the three membranes to LiCl or MgCl₂ salt solutions increased drastically with the increase of coating time. As mentioned above that mesopores existed in our BTESE networks, repeatedly coating may cover and repair the mesopore-induced defects on the hybrid silica separation layer, resulting in the improvement of salt rejections. In addition, under the same applied transmembrane pressure, M1–400, M2–400 and M3–400 all exhibited high rejections to LiCl solution and low rejections to MgCl₂ solution. This result was similar to that of the single-coated membranes, confirming that the separation mechanism would not change with the increase of coating time.

The as-prepared membranes showed the optimal salt rejections to both LiCl and MgCl₂ solutions, when the applied transmembrane pressure was 0.6 MPa. The similar rejections of M1–400, M2–400 and M3–400 to LiCl or MgCl₂ solutions were found if the applied transmembrane pressure was above 6 bar. When operated at applied transmembrane pressure of 0.6 MPa, the salt rejections of M3–400 to LiCl and MgCl₂ solutions were 74.7% and 20.3%, respectively. This phenomenon could be ascribed to the relationship between water flux and concentration polarization modulus. We deduced that when the pressure was below 0.6 MPa, the dominant effect of salt rejection is diffusion. It is believed that rejection in NF process may increase with the increase of applied pressure at a relatively low transmembrane pressure range, because water flux can increase proportionally to the difference of the applied pressure and the osmotic pressure while the amount of solute passed through the membrane did not significantly increase [37]. When the pressure was above 0.6 MPa, the convection effect was predominant in the NF process. With relatively high pressure, the improved water flux promoted the convection transport of solute. In addition, the higher pressure resulted in the increase of the concentration polarization in the boundary layer and the consequent increase of solute convection rate. As a result, the rejections in our system could reach to their stable states ultimately, which agreed with a previous report by Zhang *et al.* [38].

To study the stability of M3–400 membrane, NF experiment of the membrane was tested for 8 h at 0.6 MPa to 2 mmol·L⁻¹ LiCl solution. As shown in Fig. 13, permeabilities and rejections of the M3–400 membrane almost kept the same (91 L·m⁻²·h⁻¹·MPa⁻¹ and 74%) with some negligible fluctuations within the operation time. This result

**Fig. 13.** Rejections and permeabilities of M3–400 membrane to 2 mM LiCl solution for 8 h at 6 bar.

indicates that the as-prepared NF membrane has a good stability for long time running.

Table 4 summarizes the permeabilities and the rejections to MgCl₂ and LiCl of reported NF membranes in literatures and M3–400 prepared in this study. We note that NF performance for salt rejection is dominated by a complicated synergetic effect (*e.g.* diffusion, convection, electromigration and *etc.*) [39], and different combinations of operation parameters and membrane materials may lead to different salt separation performance. To achieve the goal of extracting lithium from high Mg²⁺/Li⁺ ratio brine lake, ideal NF process should offer state-of-the-art selectivity (*i.e.* a large absolute difference in rejection rates between LiCl and MgCl₂) and permeability. Based on such criterion, the as-prepared M3–400 operated at 0.6 MPa exhibits excellent permeability (95 L·m⁻²·h⁻¹·MPa⁻¹) and relatively high selectivity (R[LiCl]-R[MgCl₂] = 49.9%), compared with LiCl and MgCl₂ separation performance of those membranes listed in Table 4. In this work, we studied the Li⁺/Mg²⁺ separation performance of the as-prepared membranes based on the ideal single-component experiments, and further efforts are needed for the mixed solutions in the near future.

4. Conclusions

In summary, BTESE-derived silica NF membranes with negative surface charge were successfully prepared by sol-gel method through a dip-coating process for lithium extraction. BTESE-derived sol with a mean particle size of ~5 nm was used for membrane preparation and the effect of calcination temperature on the BTESE-derived organic-inorganic hybrid silica networks were compared. As evidenced by N₂

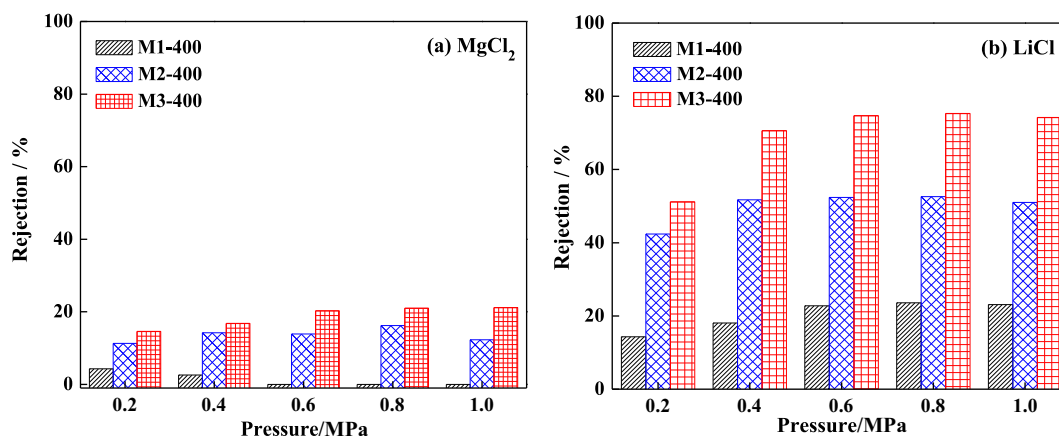
**Fig. 12.** Rejections of the M1–400, M2–400 and M3–400 membranes to (a) MgCl₂ and (b) LiCl as a function of the transmembrane pressure.

Table 4
Comparison of the MgCl₂ and LiCl separation performance of NF membranes

Membranes	Concentration/mol·L ⁻¹		Permeability/L·m ⁻² ·h ⁻¹ ·MPa ⁻¹	Rejection/%		References
	MgCl ₂	LiCl		MgCl ₂	LiCl	
DK-1812	0.063	0.0016	9.0	96	85	[40]
PA-B2-E3	0.099	0.0144	6.0	84.6	68.1	[41]
PBI	0.0034	0.0034	19.5	84	25	[42]
NF90-2540	0.14	0.0086	7.0	100	15	[43]
DAPP/TMC-PAN	0.021	0.0024	28.0	70.4	21.8	[44]
MPD/TMC-PPESK	2.0	2.0	13.4	96.5	99.1	[45]
M3-400	0.002	0.002	95	23.5	73.4	This work

Note: DK-1812: spiral-wound DK-1812model with the membrane core model of 3B02S-DAC8-1812; PA-B2-E3: Polyamide composite NF membrane with 2% branched poly (ethylene imine) and 3% ethylenediaminetetraacetic acid; PBI: polybenzimidazole nanofiltration membrane; NF90-2540: NF90-2540 (F6749226) purchased from Filmtec (DOW, USA); DAPP/TMC-PAN: interfacial polymerization of 1,4-bis(3-aminopropyl) piperazine and trimesoyl chloride on the polyacrylonitrile ultrafiltration hollow fiber membrane; MPD/TMC-PPESK: interfacial polymerization of m-phenylene diamine and trimesoyl chloride on poly(phthalazinone ether sulfone ketone).

adsorption–desorption experiments, calcinating BTESE-derived silica membranes at 200, 300 and 400 °C could produce microporous structures with pore size mainly distributed in the range of 0.5–2 nm corresponding to the pore size characteristics of typical NF membranes. The chemical states of the membranes prepared at the three temperatures were similar, while a higher calcination temperature led to a narrower pore size distribution due to the enhanced dehydroxylation and thermal degradation of the organic bridge groups in BTESE-derived networks. Zeta-potential measurements confirmed that the as-prepared BTESE-derived silica membranes displayed higher negative charge density in LiCl solution than that in MgCl₂ solution. All single-coated membranes calcined at 200, 300 and 400 °C exhibited similar permeabilities in terms of pure water, 2 mmol·L⁻¹ LiCl solution or 2 mmol·L⁻¹ MgCl₂ solution, and poor rejections to either LiCl solution or MgCl₂. Under transmembrane pressure of 6 bar, the rejections of BTESE-derived membranes calcinated at 400 °C could significantly promote from 22.8% to 74.7% when the coating time increases from one to three. We found all the prepared membranes showed higher LiCl rejection than MgCl₂ rejection, which demonstrated that Donnan exclusion effect was the predominant mechanism in salt rejection. Our optimal M3-400 could exhibit an excellent permeability of 9.50 L·m⁻²·h⁻¹·bar⁻¹ and relatively high selectivity to LiCl and MgCl₂ solutions (R[LiCl] = 74.7% and R[MgCl₂] = 20.3%) at a transmembrane pressure of 6 bar. Therefore, the negatively charged BTESE-derived silica NF membranes may offer an efficient tool for lithium extraction in practical applications.

Acknowledgments

This work is supported by the National Natural Science Foundation of China (21490581), the China Petroleum and Chemical Corporation Limited Project (317008-6) and the Innovation Driven Development Special Fund Project of Guangxi Province (AA17204092) and the Project of Priority Academic Program Development of Jiangsu Higher Education Institutions (PAPD).

References

- Z. Khalkhali, B.E. Yekta, V.K. Marghussian, Mechanical and chemical properties of Zr and P-doped lithium disilicate glass ceramics in dental restorations, *Int. J. Appl. Ceram. Technol.* 9 (2012) 497–506.
- G.A. Appleby, C.M. Bartle, G.V.M. Williams, et al., Lithium borate glass ceramics as thermal neutron imaging plates, *Curr. Appl. Phys.* 6 (2006) 389–392.
- B. Scrosati, Power sources for portable electronics and hybrid cars: Lithium batteries and fuel cells, *Chem. Rec.* 5 (2005) 286–297.
- Y. Xie, C. Wu, Design of nanoarchitected electrode materials applied in new-generation rechargeable lithium ion batteries, *Dalton Trans.* 45 (2007) 5235–5240.
- W. Xiang, S. Liang, Z. Zhou, et al., Extraction of lithium from salt lake brine containing borate anion and high concentration of magnesium, *Hydrometallurgy* 166 (2016) 9–15.
- M. Zheng, X. Liu, Lithium resource of China, *Advanced materials industry* 8 (2007) 13–16(In Chinese).
- A. Somrani, A.H. Hamzaoui, M. Pontie, Study on lithium separation from salt lake brines by nanofiltration (NF) and low pressure reverse osmosis (LPRO), *Desalination* 317 (2013) 184–192.
- M. Grágeda, A. González, M. Grágeda, et al., Purification of brines by chemical precipitation and ion-exchange processes for obtaining battery-grade lithium compounds, *Int. J. Energy Res.* 13 (2018) 2386–2399.
- T. Hoshino, Preliminary studies of lithium recovery technology from seawater by electro dialysis using ionic liquid membrane, *Desalination* 317 (2013) 11–16.
- L. Gong, W. Ouyang, Z. Li, et al., Direct numerical simulation of continuous lithium extraction from high Mg²⁺/Li⁺ ratio brines using microfluidic channels with ion concentration polarization, *J. Membr. Sci.* 556 (2018) 34–41.
- M. Chen, Wu R, Ju S, et al., Improved performance of Al-doped LiMn₂O₄ ion-sieves for Li⁺, adsorption, *Microporous Mesoporous Mater.* 261 (2018) 29–34.
- A. Pérez-González, R. Ibáñez, P. Gómez, et al., Nanofiltration separation of poly-valent and mono-valent anions in desalination brines, *J. Membr. Sci.* 473 (2015) 16–27.
- X. Chen, M. Qiu, H. Ding, et al., Reduced graphene oxide nanofiltration membrane intercalated by well-dispersed carbon nanotubes for drinking water purification, *Nanoscale* 10 (2016) 5696–5705.
- Xu P, W. Wang, X. Qian, et al., Positive charged PEI-TMC composite nanofiltration membrane for separation of Li⁺ and Mg²⁺ from brine with high Mg²⁺/Li⁺ ratio, *Desalination* 449 (2019) 57–68.
- G. Yang, H. Shi, W. Liu, et al., Investigation of Mg²⁺/Li⁺ separation by nanofiltration, *Chin. J. Chem. Eng.* 4 (2011) 586–591.
- Q. Bi, Z. Zhang, C. Zhao, Study on the recovery of lithium from high Mg²⁺/Li⁺ ratio brine by nanofiltration, *Water Science & Technology* 10 (2014) 1690–1694.
- C. Wu, S. Zhang, D. Yang, et al., Preparation, characterization and application in wastewater treatment of a novel thermal stable composite membrane, *J. Membr. Sci.* 279 (2006) 238–245.
- X.Q. Cheng, Y. Liu, Z. Guo, et al., Nanofiltration membrane achieving dual resistance to fouling and chlorine for “green” separation of antibiotics, *J. Membr. Sci.* 493 (2015) 156–166.
- D. Menne, C. Üzümlü, A. Koppelman, et al., regenerable polymer/ceramic hybrid nanofiltration membrane based on polyelectrolyte assembly by layer-by-layer technique, *J. Membr. Sci.* 520 (2016) 924–932.
- M. Kanezashi, K. Yada, T. Yoshioka, et al., Organic–inorganic hybrid silica membranes with controlled silica network size: Preparation and gas permeation characteristics, *J. Membr. Sci.* 348 (2010) 310–318.
- X. Rong, J. Wang, M. Kanezashi, et al., Development of robust organosilica membranes for reverse osmosis, *Langmuir* 27 (2011) 13996–13999.
- K. Oda, K. Akamatsu, T. Sugawara, et al., Dehydrogenation of methylcyclohexane to produce high-purity hydrogen using membrane reactors with amorphous silica membranes, *Ind. Eng. Chem. Res.* 49 (2010) 11287–11293.
- K. Maver, U.L. Tangar, P. Judeinstein, et al., Dynamic studies of Ormosil membranes, *J. Non-Cryst. Solids* 354 (2008) 680–687.
- H. Song, S. Zhao, J. Lei, et al., Pd-doped organosilica membrane with enhanced gas permeability and hydrothermal stability for gas separation[J], *J. Mater. Sci.* 51 (2016) 6275–6286.
- W. Puthai, M. Kanezashi, H. Nagasawa, et al., Effect of firing temperature on the water permeability of SiO₂-ZrO₂ membranes for nanofiltration, *J. Membr. Sci.* 497 (2016) 348–356.
- Yu S, T.K.S. Wong, H. Xiao, et al., The comparison of thermal and dielectric properties of silsesquioxane films cured in nitrogen and in air, *Chem. Phys. Lett.* 380 (2003) 111–116.
- H. Song, Y. Wei, C. Wang, et al., Tuning sol size to optimize organosilica membranes for gas separation, *Chin. J. Chem. Eng.* 26 (2018) 53–59.
- P.H.T. Ngamou, J.P. Overbeek, R. Kreiter, et al., Plasma-deposited hybrid silica membranes with a controlled retention of organic bridges, *J. Mater. Chem. A* 18 (2013) 55–67.
- C. Visvanathan, P.K. Roy, Potential of nanofiltration for phosphate removal from wastewater, *Environ. Technol. Lett.* 18 (1997) 551–556.
- A. Seidel, J.J. Waypa, M. Elimelech, Role of charge (Donnan) exclusion in removal of arsenic from water by a negatively charged porous nanofiltration membrane, *Environ. Eng. Sci.* 18 (2001) 105–113.

- [31] X. Yang, L. Yan, F. Ran, et al., Interface-confined surface engineering constructing water-unidirectional Janus membrane, *J. Membr. Sci.* 576 (2019) 9–16.
- [32] H. Suna, Y. Zhanga, H. Sadama, et al., Novel mussel-inspired zwitterionic hydrophilic polymer to boost membrane water-treatment performance, *J. Membr. Sci.* 582 (2019) 1–9.
- [33] Y. Zhang, H. Sun, H. Sadam, et al., Supramolecular chemistry assisted construction of ultra-stable solvent-resistant membranes for angstrom-sized molecular separation, *Chem. Eng. J.* 371 (2019) 535–543.
- [34] A.G. Volkov, S. Paula, D.W. Deamer, Two mechanisms of permeation of small neutral molecules and hydrated ions across phospholipid bilayers. Bioelectrochemistry, *Bioenergetics* 42 (1997) 153–160.
- [35] J. Schaep, B.V.D. Bruggen, C. Vandecasteele, et al., Influence of ion size and charge in nanofiltration, *Sep. Purif. Technol.* 14 (1998) 155–162.
- [36] C. Wei, Z. He, L. Lin, et al., Negatively charged polyimide nanofiltration membranes with high selectivity and performance stability by optimization of synergistic imidization, *J. Membr. Sci.* 563 (2018) 752–761.
- [37] Tu K, L. Nghiem, A. Chivas, et al., Boron removal by reverse osmosis membranes in seawater desalination applications. *Separation & Purification, Technology* 75 (2010) 87–101.
- [38] Y. Zhang, L. Zhang, L. Hou, et al., Modeling of the variations of permeate flux, concentration polarization, solute rejection inside nanofiltration system, *AIChE J.* 65 (2019) 1076–1087.
- [39] X. Li, C. Zhang, S. Zhang, et al., Preparation and characterization of positively charged polyamide composite nanofiltration hollow fiber membrane for lithium and magnesium separation, *Desalination* 369 (2015) 26–36.
- [40] Q. Bi, Z. Zhang, C. Zhao, et al., Study on the recovery of lithium from high Mg^{2+}/Li^{+} ratio brine by nanofiltration, *Water Science & Technology* 70 (2014) 1690–1694.
- [41] W. Li, C. Shi, A. Zhou, et al., A positively charged composite nanofiltration membrane modified by EDTA for $LiCl/MgCl_2$ separation, *Sep. Purif. Technol.* 186 (2017) 233–242.
- [42] K.Y. Wang, Y. Xiao, T.S. Chung, Chemically modified polybenzimidazole nanofiltration membrane for the separation of electrolytes and cephalexin, *Chem. Eng. Sci.* 61 (2006) 5807–5817.
- [43] A. Somrani, A.H. Hamzaoui, M. Pontie, Study on lithium separation from salt lake brines by nanofiltration (NF) and low pressure reverse osmosis (LPRO), *Desalination* 317 (2013) 184–192.
- [44] X. Li, C. Zhang, S. Zhang, et al., Preparation and characterization of positively charged polyamide composite nanofiltration hollow fiber membrane for lithium and magnesium separation, *Desalination* 369 (2015) 26–36.
- [45] C. Wu, S. Zhang, D. Yang, et al., Preparation, characterization and application in wastewater treatment of a novel thermal stable composite membrane, *J. Membr. Sci.* 279 (2006) 238–245.